applied sciences

MDPI

Article

Optimal Interplanetary Transfer of Solar Wind Ion Focusing Thruster-Based Spacecraft

Alessandro A. Quarta *, Lorenzo Niccolai, Giovanni Mengali and Marco Bassetto

Department of Civil and Industrial Engineering, University of Pisa, 56122 Pisa, Italy
* Correspondence: alessandro.antonio.quarta@unipi.it

Abstract: The Solar Wind Ion Focusing Thruster (SWIFT) is a highly-innovative propellantless propulsion concept, recently proposed by Gemmer and Mazzoleni. In its nominal configuration, a SWIFT consists of a conically-shaped mesh of positively-charged conducting tethers, with its vertex linked to the spacecraft and its axis oriented towards the Sun. The SWIFT collects and filters the solar wind plasma and suitably directs the positive ions, which are then accelerated by an ion thruster. Such a device is theoretically able to generate a deep-space propulsive acceleration that comes, in part, from the solar wind dynamic pressure impinging on the conical grid and, in part, from the positive ion beam. In particular, the orientation of the ion beam may be chosen in such a way as to set the resultant propulsive acceleration and steer the spacecraft. The aim of this paper is to analyze the performance of a SWIFT-propelled spacecraft in an orbit-to-orbit two-dimensional interplanetary transfer. To that end, some mission scenarios are studied, in an optimal framework, by minimizing the total flight time necessary for the spacecraft to complete the transfer as a function of the propulsion system performance parameters. Numerical simulations are used to compare the optimal flight times calculated in simplified Earth–Venus and Earth–Mars transfers with those obtained by considering other propellantless propulsion systems.

Keywords: Solar Wind Ion Focusing Thruster; optimal transfer; heliocentric mission analysis

Citation: Quarta, A.A.; Niccolai, L.; Mengali, G.; Bassetto, M. Optimal Interplanetary Transfer of Solar Wind Ion Focusing Thruster-Based Spacecraft. *Appl. Sci.* **2023**, *13*, 3820. https://doi.org/10.3390/app13063820

Academic Editors: Jason Cassibry and Nathan Schilling

Received: 29 December 2022
Revised: 10 March 2023
Accepted: 15 March 2023
Published: 16 March 2023

1. Introduction

Propellantless systems are the frontier of current and near-term technology for space propulsion and are likely to become the only viable way to realize new advanced mission concepts, such as reaching high-energy orbits of comets [1,2] or Solar System small bodies [3–5], rectilinear trajectories [6,7], displaced orbits [8–11], or the creation and maintenance of artificial Lagrangian points [12–14] and hovering conditions over asteroids [15]. Solar sails and electric solar wind sails (E-sails) are currently the most promising types of propellantless systems. They are both able to gain energy from the Sun, although with different physical mechanisms. On one side, solar sails are propelled by the momentum transfer of solar photons impinging on a large, lightweight, and reflecting membrane [16–20]. E-sails, instead, produce a propulsive thrust by extracting momentum from the solar wind ions, which are shielded by an electric field generated around a large grid of conducting tethers [21,22]. Despite their different working principles, the common feature of solar sails and E-sails is that both require large surfaces to produce thrust and that those surfaces must be suitably oriented with respect to the Sun–spacecraft (that is, radial) direction to generate a thrust component capable of modifying the spacecraft orbital momentum [16,23,24]. Their other common feature is that the maximum thrust magnitude, for a given distance from the Sun, is obtained when the reference plane (either the reflecting membrane or the nominal plane containing the conducting tethers) is placed normal to the radial direction [25].

The need to reorient the reference plane for guidance and navigation purposes gives rise to a double issue. In the first place, the rotations of the plane may represent a complex task to carry out, especially when large reorientation angles are involved. However, even

more important is the propulsive effect caused by the rotation, since, as the reference plane strays from a Sun-facing orientation, the solar wind ions and photons "see" a smaller surface to hit, with a consequent reduction of thrust magnitude. Alternative configurations have been proposed to mitigate these drawbacks. For example, in the case of photonic propulsion systems, the functions of collecting and directing the solar radiation may be separated by means of an arrangement that is called Solar Photon Thrustor (SPT), according to its original definition by Robert Forward [26]. In that system, the solar rays impinging on a collector (a large curved reflecting surface) are first directed on a small flat mirror, the reflector, which redirects them on a second steerable mirror, the director, used to suitably orient the force acting on the SPT. Since the collector is always oriented orthogonal to the Sun-pointing direction, it always produces the maximum allowable thrust magnitude for a given collector reflecting surface. Due to its special arrangement, a typical SPT configuration is, in principle, superior to a conventional solar sail, as it may be concluded from simulations of Earth escape trajectories [27] or interplanetary trajectories [28,29]. Updated results, made on realistic SPT configurations, have however called into question the actual effectiveness of this advanced propulsion concept [30].

Returning to systems that extract momentum from the solar wind ions, the Solar Wind Ion Focusing Thruster (SWIFT) is a new propellantless device, which may be thought of as an evolution of the E-sail concept [31–33]. It essentially consists of a grid of conducting tethers, electrostatically charged at a positive electric potential, arranged in a conically-shaped mesh with a circular base that has a radius of some kilometers and is supported by a few auxiliary booms with stiffening purposes. The solar wind ions are filtered by the charged SWIFT cone and the collected positive ions are accelerated by an ion thruster and then ejected in a beam that can be suitably oriented to provide the desired thrust component. The propulsion system also includes a cathode (or other suitable electron source) to prevent the thruster from accumulating a net charge. Since the SWIFT cone axis always points to the Sun, the functions of collecting and directing the solar wind ions are separated, and for this reason the SWIFT concept has interesting similarities with the Forward's SPT configuration. So far, however, a reasonable estimate of the SWIFT capabilities is still lacking and is confined to the preliminary analysis in Ref. [34], where Gemmer et al. have reported some parametric studies about flyby missions to Venus and Mars. The aim of this paper is to fill that gap and quantify the SWIFT's performance in a systematic way, by translating the analysis into the solution of a minimum-time interplanetary transfer problem. In this case, the optimal (i.e., minimum-time) trajectories are obtained with an indirect approach by enforcing the necessary conditions for optimality according to the Pontryagin's maximum principle [35]. In particular, the Hamiltonian associated to the problem is maximized at any time by maximizing the projection of the propulsive acceleration vector along the direction of the Lawden's primer vector [36,37].

This paper is organized as follows. The next section describes the spacecraft dynamics in a heliocentric mission scenario and provides an extension of the thrust model recently discussed in Ref. [34]. The analytic expression of the spacecraft propulsive acceleration vector is then used in Section 3 to optimize the spacecraft transfer trajectory in a circle-to-circle coplanar orbit transfer, while Section 4 discusses the optimal results obtained by numerically simulating two potential (and simplified) interplanetary missions towards Mars and Venus. Finally, the last section summarizes and highlights the main outcomes of this work.

2. Mathematical Model

The performance of a SWIFT-based spacecraft is here investigated assuming that the mission consists of a heliocentric transfer trajectory between two circular and coplanar orbits. Such a two-dimensional spacecraft motion may be conveniently described with the aid of a heliocentric polar reference frame $\mathcal{T}(O; r, \theta)$, whose origin O coincides with the Sun's center of mass; r is the Sun–spacecraft distance, and θ is the spacecraft polar angle

measured counterclockwise from a fixed direction, which coincides with the Sun–spacecraft line at the initial time $t = t_0 \triangleq 0$; see Figure 1.

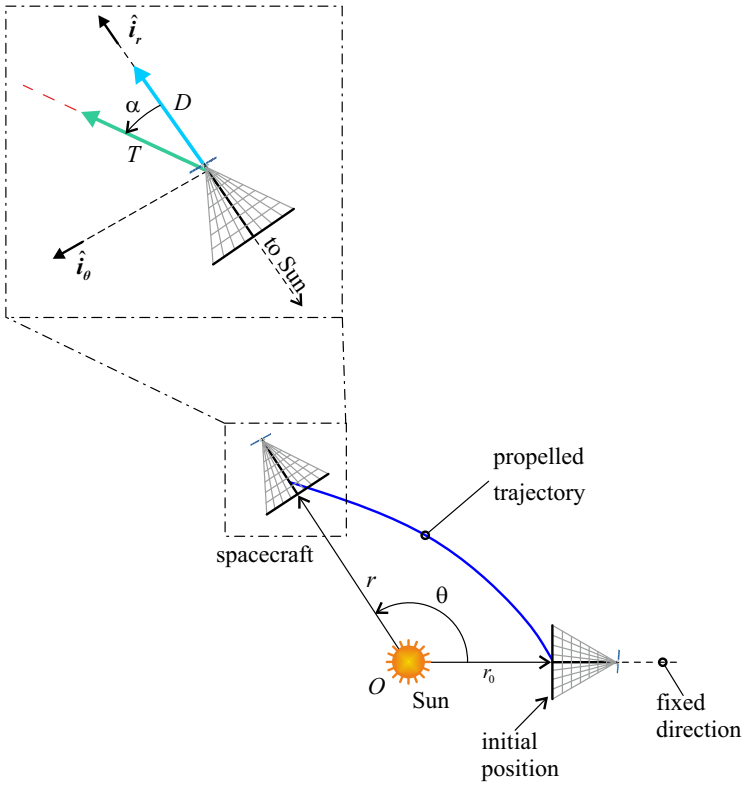

Figure 1. Sketch of the polar reference frame and SWIFT-induced thrust contributions.

The fundamental unit vectors of $\mathcal{T}$ are denoted by $\{\hat{\boldsymbol{i}}_r, \hat{\boldsymbol{i}}_\theta\}$, where $\hat{\boldsymbol{i}}_r$ is the outward radial unit vector, and $\hat{\boldsymbol{i}}_\theta$ is the circumferential unit vector, so that the spacecraft position ($\boldsymbol{r}$) and velocity ($\boldsymbol{v}$) vectors can be written in $\mathcal{T}$ as

$$\boldsymbol{r} = r\,\hat{\boldsymbol{i}}_r \quad , \quad \boldsymbol{v} = v_r\,\hat{\boldsymbol{i}}_r + v_\theta\,\hat{\boldsymbol{i}}_\theta, \tag{1}$$

where v_r (or v_θ) is the radial (or circumferential) component of $\boldsymbol{v}$. In the polar reference frame, the SWIFT-induced propulsive acceleration is written as a function of the radial (a_r) and circumferential (a_θ) components as

$$\boldsymbol{a} = a_r\,\hat{\boldsymbol{i}}_r + a_\theta\,\hat{\boldsymbol{i}}_\theta, \tag{2}$$

so that the spacecraft equations of motion are

$$\dot{r} = v_r \tag{3}$$

$$\dot{\theta} = \frac{v_\theta}{r} \tag{4}$$

$$\dot{v}_r = \frac{v_\theta^2}{r} - \frac{\mu_\odot}{r^2} + a_r \tag{5}$$

$$\dot{v}_\theta = -\frac{v_r\,v_\theta}{r} + a_\theta, \tag{6}$$

where the dot symbol denotes a derivative with respect to time t, and $\mu_\odot$ is the Sun's gravitational parameter. The resultant (spacecraft) heliocentric trajectory requires a suitable model describing the SWIFT-induced propulsive acceleration components as a function of

the solar wind properties and of the propulsion system design parameters. Such a model is illustrated in the next section.

Thrust Vector Description

According to Refs. [31–33], the SWIFT propulsion system concept consists of a conically-shaped mesh grid of conducting tethers, which are electrostatically charged with a nominal positive voltage ϕ_0, and a few auxiliary booms, used as supporting structural elements, as illustrated in Figure 2, where δ is the cone aperture angle.

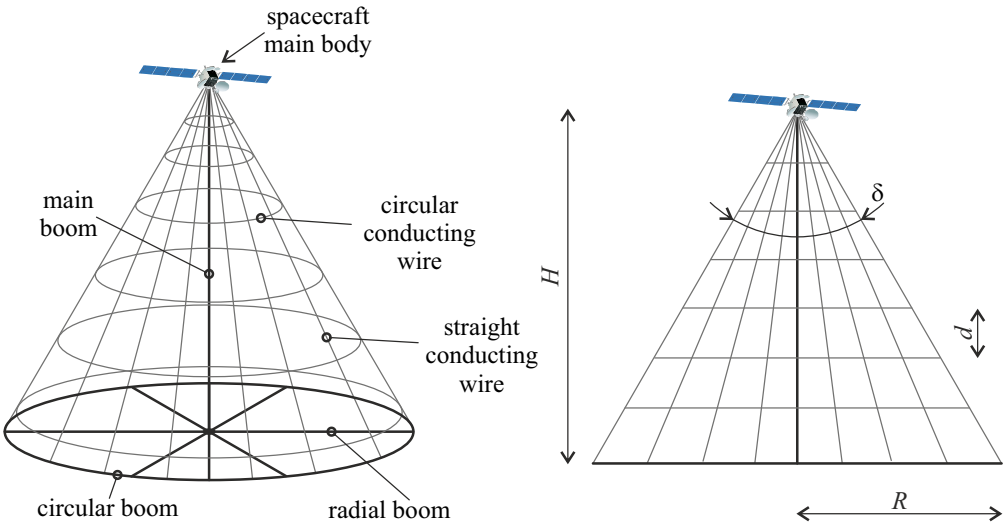

(**a**) Spacecraft main elements. (**b**) Geometric design parameters.

Figure 2. Conceptual scheme of a SWIFT-based spacecraft (main body not to scale).

The solar wind dynamic pressure impinging on the conically-shaped mesh grid of the SWIFT produces a propulsive force component D, usually referred to as "drag" because it opposes the Sun's gravitational pull, which is aligned with the outward radial direction $\hat{\boldsymbol{\imath}}_r$ (see Figure 1), and given by [34]

$$D = n_{\mathrm{sw}}\, m_p\, v_{\mathrm{sw}}^2\, A, \tag{7}$$

where n_{sw} and v_{sw} are the local solar wind particle density and bulk velocity, respectively, m_p is the proton mass, $A \triangleq \pi R^2$ denotes the SWIFT cone base area, R being the cone's base radius. The latter is here considered a geometric design parameter. The values of m_p and v_{sw}, along with other physical parameters later defined and used in the numerical simulations, are reported in Table 1.

Table 1. Constants and physical parameters used in the thrust model and in numerical simulations.

Parameter	Value	Units
e	$1.60217663 \times 10^{-19}$	C
m_e	$9.1093837 \times 10^{-31}$	kg
m_p	$1.67262192 \times 10^{-27}$	kg
$n_\oplus$	7.3×10^6	particles/m^3
$r_\oplus$	1	au
v_{sw}	400	km/s
$\mu_\odot$	132,712,439,935.5	km^3/s^2
ρ_w	2700	kg/m^3

There exists a second contribution to the SWIFT-induced total force [34], that is, the steerable component T of Figure 1, obtained by accelerating the collected solar wind positive ions and then ejecting them in a beam that can be suitably oriented by means of a dedicated assembly. In a two-dimensional mission scenario, the orientation of the ion beam (an so the direction of T) is defined by a single reference angle α, that is, the thrust angle, where $\alpha \in [-\alpha_{\max}, \alpha_{\max}]$ (with $\alpha_{\max} > 0$) is measured counterclockwise from $\hat{\boldsymbol{i}}_r$ as illustrated in Figure 1. Note that α is constrained to a maximum ($\alpha_{\max}$) and a minimum ($-\alpha_{\max}$) value by the presence of the conical structure. Bearing in mind the scheme of Figure 2b, the maximum thrust angle cannot exceed π rad $- \delta/2$, while in the rest of the paper $\alpha_{\max}$ is calculated as

$$\alpha_{\max} = \pi \,\text{rad} - \frac{\delta}{2} - \Delta\alpha, \tag{8}$$

where $\Delta\alpha \geq 0$ is a contingency factor that is added to the nominal value of $(\pi \,\text{rad} - \delta/2)$ to account for possible uncertainties on the SWIFT cone geometry. According to Ref. [34], the magnitude of T is given by

$$T = n_{\text{sw}}\, m_p\, v_{\text{sw}}\, v_{\text{ex}}\, A \equiv n_{\text{sw}}\, m_p\, v_{\text{sw}}\, v_{\text{ex}}\, \pi\, R^2, \tag{9}$$

where v_{ex} is the ion beam exhaust velocity so that, from Equations (7) and (9), it can be observed that the steerable thrust and the drag are related by the simple relation

$$T = k\, D, \tag{10}$$

where

$$k \triangleq \frac{v_{\text{ex}}}{v_{\text{sw}}}. \tag{11}$$

In a preliminary mission analysis, the solar wind velocity v_{sw} can be assumed to be practically constant, that is, nearly independent of both r and t. This means that the value of k, defined in Equation (11), may be modified by simply varying the ion beam exhaust velocity v_{ex}. In this sense, k is here considered a propulsive design parameter. Since the particle density n_{sw} scales as the inverse square of the heliocentric distance, that is,

$$n_{\text{sw}} = n_{\oplus}\left(\frac{r_{\oplus}}{r}\right)^2, \tag{12}$$

where $r_{\oplus} = 1$ au is a reference distance and $n_{\oplus}$ the solar wind particle density at $r = r_{\oplus}$, the force components D and T may be written in a compact form as

$$D = D_{\oplus}\left(\frac{r_{\oplus}}{r}\right)^2 \tag{13}$$

$$T = k\, D_{\oplus}\left(\frac{r_{\oplus}}{r}\right)^2, \tag{14}$$

where $D_{\oplus}$ denotes the value of D calculated at $r = r_{\oplus}$. Note that the previously described model assumes that the solar wind density is stationary, i.e., that it does not fluctuate over time. This simplifying assumption is reasonable in a preliminary mission analysis, although data collected by several space missions [38–40] clearly indicate that the plasma parameters undergo chaotic temporal fluctuations. Using Equation (7), the expression of $D_{\oplus}$ is

$$D_{\oplus} \triangleq n_{\oplus}\, m_p\, v_{\text{sw}}^2\, \pi\, R^2, \tag{15}$$

which is a function of the (geometric) design parameter R. To obtain the expressions of the propulsive acceleration components $\{a_r, a_\theta\}$ in Equation (2), the reference drag force $D_{\oplus}$ is rewritten in terms of force-to-mass ratio as

$$a_{D_{\oplus}} \triangleq \frac{D_{\oplus}}{m}, \tag{16}$$

where m is the total spacecraft mass, here considered as a constant.

The value of m may be estimated with a spacecraft mass breakdown model. To that end, we adopted the original approach reported in Ref. [34], which has been suitably refined and extended. More precisely, the total spacecraft mass is considered as the sum of four contributions, that is,

$$m = m_w + m_s + m_{\mathrm{ps}} + m_b, \tag{17}$$

where m_w is the total mass of conducting wires, m_s is the total mass of supporting booms, m_{ps} is the mass of the power generation subsystem, and m_b is the mass of the main spacecraft, including the payload and the other typical subsystems. In this analysis, m_b is a sort of inertial design parameter that depends on the characteristics of the scientific mission to be fulfilled. The total mass of the conducting wires composing the (conical) mesh grid is evaluated as

$$m_w = \pi \, \rho_w \, r_w^2 \, L_w, \tag{18}$$

where ρ_w is the density of the wire material, r_w is the wire radius, and L_w is the total length of the conducting wires. The latter is the sum of the total length of the straight wires and the circular wires, viz.

$$L_w = \left[\frac{N_e \, R}{\sin(\delta/2)} + 2 \, \pi \, d \tan(\delta/2) \sum_{i=1}^{N_c} i \right], \tag{19}$$

where N_e and N_c are the number of external (straight) and circular conducting wires, respectively, and d is the spacing distance between two consecutive circular wires; see Figure 2. Unlike N_e, which is a design parameter, N_c is calculated as

$$N_c = \mathrm{ceil}\left[\frac{R}{d \, \tan(\delta/2)} \right], \tag{20}$$

where $\mathrm{ceil}(x)$ denotes the ceil function of the argument x, which gives a smaller integer number greater than x.

The second contribution to the total spacecraft mass is given by the structural elements necessary to support the SWIFT, that is, m_s. According to Gemmer et al. [31], the supporting structure comprises a main boom, which extends from the spacecraft's main body to the cone base, a ring-shaped structure around the cone base, and a number N_s of auxiliary radial elements connecting the main boom and the base ring; see Figure 2. The total length L_s of the supporting structural elements is therefore given by

$$L_s = 2 \, \pi \, R + \frac{R}{\tan(\delta/2)} + N_s \, R, \tag{21}$$

so that

$$m_s = \rho_{lb} \, L_s, \tag{22}$$

where ρ_{lb} is the linear mass density of the structural elements. The mass m_{ps} of the power generation subsystem is estimated by writing the total electric power P required by the spacecraft as a function of the design parameters. To this end, two main contributions are accounted for, that is, the electric power P_{ex} used to accelerate the (steerable) ion beam, and the electric power P_w required to maintain the conical grid voltage, viz.

$$P = P_{\mathrm{ex}} + P_w, \tag{23}$$

in which the value of P_{ex} is calculated as

$$P_{\mathrm{ex}} = \frac{1}{2} \, n_{\oplus} \, m_p \, A \, v_{\mathrm{sw}} \, v_{\mathrm{ex}}^2 \equiv \frac{1}{2} \, n_{\oplus} \, m_p \, \pi \, R^2 \, v_{\mathrm{sw}}^3 \, k^2, \tag{24}$$

while P_w is given by

$$P_w = 2\, n_\oplus\, r_w \sqrt{\frac{2\, e^3\, \phi_0^3}{m_e}}\, L_w, \tag{25}$$

where e is the elementary charge, m_e is the electron mass, and L_w is obtained from Equation (19). Note that the power consumption estimation involves the solar wind ion density at Sun–Earth distance, so it is valid as long as the Sun–spacecraft distance is not too far from 1 au. Finally, the mass of the power generation system $m_{\rm ps}$ is considered a linear function [31] of P through the (assigned) power subsystem specific mass β, that is,

$$m_{\rm ps} = \beta\, P \equiv \beta \left(\frac{1}{2}\, n_\oplus\, m_p\, \pi\, R^2\, v_{\rm sw}^3\, k^2 + 2\, n_\oplus\, r_w \sqrt{\frac{2\, e^3 \phi_0^3}{m_e}}\, L_w \right). \tag{26}$$

Note that, in the right hand side of Equation (26), the dependence on the base radius R also appears in L_w; see Equation (19).

Based on the previous discussion, the two propulsive acceleration components $\{a_r, a_\theta\}$ can be calculated using Equations (7), (9) and (17), recalling that the drag force component D is radial, while the steerable thrust component T forms an angle α with $\hat{\boldsymbol{i}}_r$; see Figure 1. The expressions of $\{a_r,\, a_\theta\}$ are therefore

$$a_r = \frac{D + T\, \cos\alpha}{m} \equiv a_{D_\oplus} \left(\frac{r_\oplus}{r} \right)^2 (1 + k\, \cos\alpha) \tag{27}$$

$$a_\theta = \frac{T\, \sin\alpha}{m} \equiv a_{D_\oplus} \left(\frac{r_\oplus}{r} \right)^2 k\, \sin\alpha, \tag{28}$$

where $a_{D_\oplus}$ and k are given by Equations (16) and (11), respectively. The magnitude of the propulsive acceleration vector can be calculated by means of Equations (27) and (28) as

$$\|\boldsymbol{a}\| = a_{D_\oplus} \left(\frac{r_\oplus}{r} \right)^2 \sqrt{1 + k^2 + 2\, k \cos\alpha}. \tag{29}$$

Its maximum value, for a given solar distance, is obtained when $\alpha = 0$, that is, when T is aligned with the outward radial direction, so that the expression of $a_{\rm max}$ depends on the Sun–spacecraft distance as

$$a_{\rm max} = a_{D_\oplus} \left(\frac{r_\oplus}{r} \right)^2 (1 + k). \tag{30}$$

The value of $\|\boldsymbol{a}\|$ or $a_{\rm max}$ can be used to obtain the dimensionless version of the propulsive acceleration components as a function of the pair $\{\alpha,\, k\}$, viz.

$$\frac{a_r}{a_{\rm max}} = \frac{1 + k\, \cos\alpha}{1 + k} \quad , \quad \frac{a_\theta}{a_{\rm max}} = \frac{k}{1 + k}\, \sin\alpha \tag{31}$$

or

$$\frac{a_r}{\|\boldsymbol{a}\|} = \frac{1 + k\, \cos\alpha}{\sqrt{1 + k^2 + 2\, k \cos\alpha}} \quad , \quad \frac{a_\theta}{\|\boldsymbol{a}\|} = \frac{k\, \sin\alpha}{\sqrt{1 + k^2 + 2\, k \cos\alpha}}. \tag{32}$$

In this regard, Figure 3 shows the propulsive acceleration, normalized with $a_{\rm max}$, as a function of k and α.

Figure 4, instead, illustrates the dimensionless components of the propulsive acceleration as a function of α for different values of the propulsive parameter k. While the maximum value of a_r is obtained with $\alpha = 0$, the circumferential component a_θ is maximized by values of the thrust angle that vary with the design parameter k.

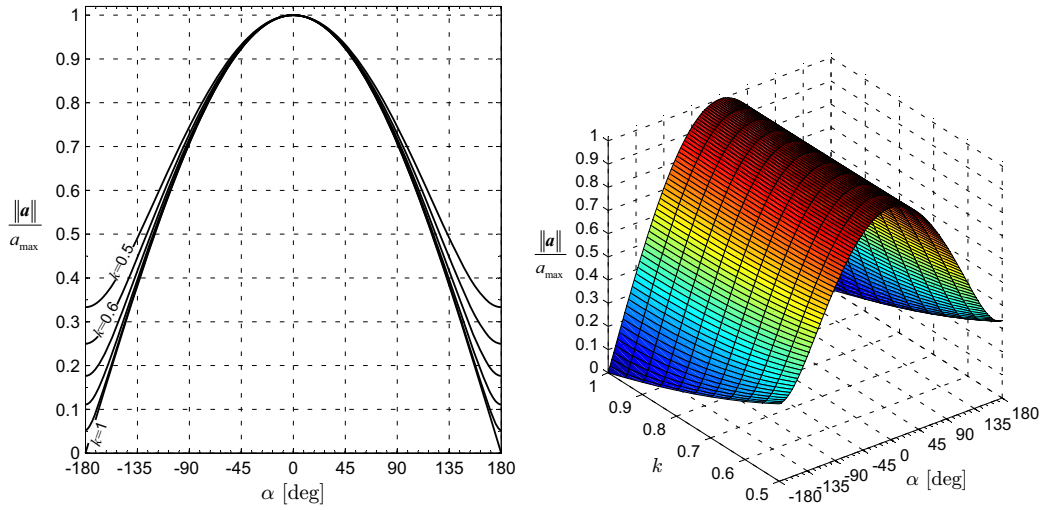

(**a**) Level curves. (**b**) Three-dimensional (3D) function surface.

Figure 3. Dimensionless propulsive acceleration magnitude as a function of α and k.

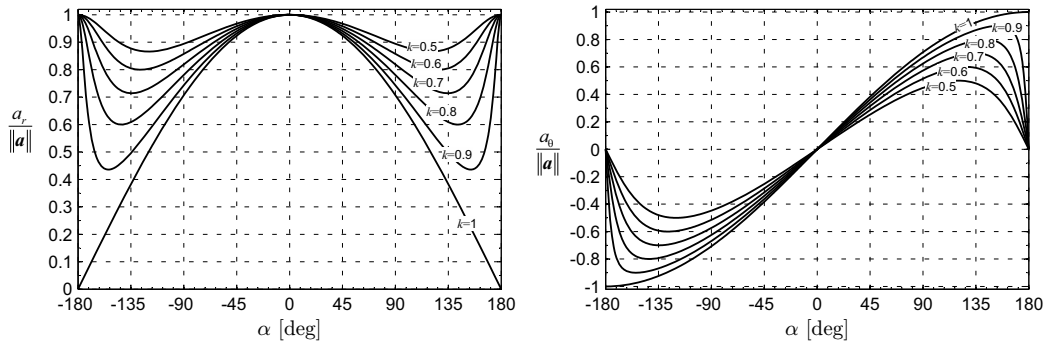

(**a**) Radial component. (**b**) Circumferential component.

Figure 4. Dimensionless radial and circumferential components of $\boldsymbol{a}$ as functions of α and k.

Finally, Figure 5 shows the classical force bubble [41] for different values of k, suggesting that a larger value of k may provide a larger circumferential component of the propulsive acceleration, with the drawback of a corresponding necessary increase of the required power for ion acceleration, as shown by Equation (24). Note that Figure 5 takes into account the presence of a conical grid with aperture angle $\delta = 60$ deg and a contingency $\Delta\alpha = 0$, thus implying that the thrust angle ranges in the interval $\alpha \in [-150, 150]$ deg.

From the viewpoint of interplanetary transfer performance, the possibility of generating a significant value of circumferential acceleration a_θ is of primary concern. In this regard, from Equation (28), the maximum value of a_θ is reached when $\alpha = 90$ deg and is given by

$$\max(a_\theta) = a_{D_\oplus}\left(\frac{r_\oplus}{r}\right)^2 k. \tag{33}$$

Bearing in mind Equation (31), it is found that

$$\frac{\max(a_\theta)}{a_{\max}} = \frac{k}{1+k}. \tag{34}$$

The preceding equation allows us to compare the thrust capabilities of the SWIFT concept and that of an ideal (i.e., perfectly reflecting) flat solar sail in terms of the dimensionless ratio $\max(a_\theta)/a_{\max}$. In fact, in an ideal solar sail (subscript ss), the circumferential component of the propulsive acceleration can be written as [16]

$$a_{\theta_{ss}} = a_{\max_{ss}} \sin\alpha_{ss} \cos^2\alpha_{ss}, \tag{35}$$

where α_{ss} is the angle between the sail thrust vector (whose direction coincides with that of the unit vector normal to the sail-shaded plane [42]) and the radial direction, while $a_{\max_{ss}}$ is the (local) maximum propulsive acceleration magnitude obtained in a Sun-facing condition [43]; see Figure 6.

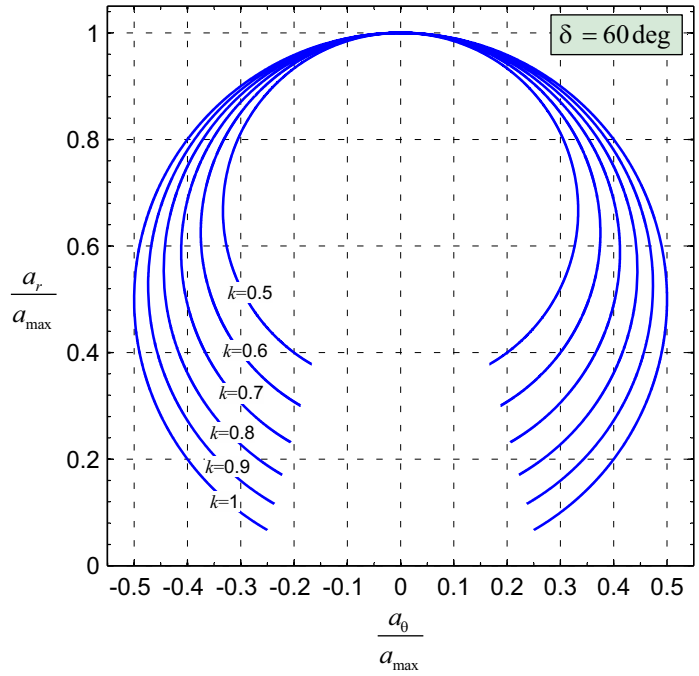

Figure 5. SWIFT force bubble with different values of k, when the cone aperture is $\delta = 60$ deg and the contingency is $\Delta\alpha = 0$.

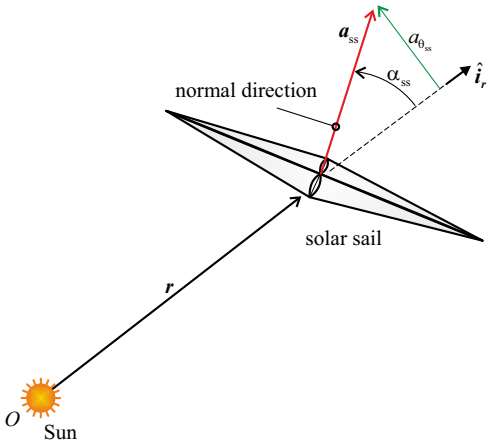

Figure 6. Ideal (photonic) flat solar sail thrust angle.

The value of $\max(a_{\theta_{ss}})/a_{\max_{ss}}$ is reached when $\alpha_{ss} = \arcsin(1/\sqrt{3})$, with

$$\frac{\max(a_{\theta_{ss}})}{a_{\max_{ss}}} = \frac{2}{3\sqrt{3}}. \tag{36}$$

Equating the right hand sides of Equations (34) and (36), one obtains the value of k necessary for the SWIFT thruster to be equal to the dimensionless circumferential component of the solar sail-induced acceleration, that is,

$$k = k^\star = \frac{2}{3\sqrt{3}-2} \simeq 0.6258. \tag{37}$$

As a result, when $k > k^\star$, the maximum value of a_θ for a SWIFT-based spacecraft is greater than the corresponding value of an ideal solar sail of equal $a_{\max}$. In the special case when $k = k^\star$, $\delta = 60$ deg and $\Delta\alpha = 0$, Figure 7 compares the force bubbles of the two propulsion systems.

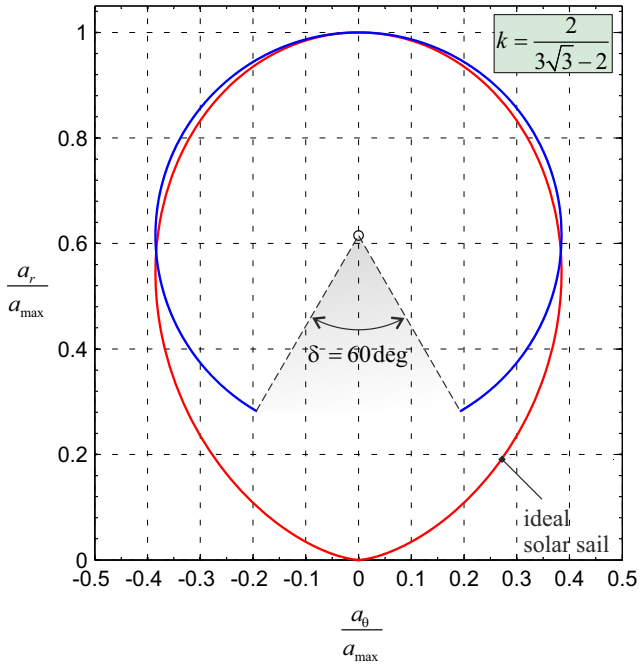

Figure 7. Comparison between the force bubble of a SWIFT and an ideal (photonic) flat solar sail when $k = k^\star$, $\delta = 60$ deg and $\Delta\alpha = 0$.

With the aid of Equations (27) and (28), the last two equations of motion (5) and (6) become

$$\dot{v}_r = \frac{v_\theta^2}{r} - \frac{\mu_\odot}{r^2} + a_{D_\oplus}\left(\frac{r_\oplus}{r}\right)^2(1 + k\,\cos\alpha) \tag{38}$$

$$\dot{v}_\theta = -\frac{v_r\,v_\theta}{r} + a_{D_\oplus}\left(\frac{r_\oplus}{r}\right)^2 k\,\sin\alpha, \tag{39}$$

in which the thrust angle α is the control variable, while $a_{D_\oplus}$ and k may be thought of as the design parameters that define the propulsive performance of the SWIFT system. For a given pair $\{a_{D_\oplus}, k\}$, the time variation of the thrust angle $\alpha = \alpha(t)$ is obtained as the solution of an optimal control problem in which the transfer trajectory minimizes the flight time between the parking and the target orbit, as discussed in the next section.

3. Trajectory Optimization

Consider a circle-to-circle (coplanar) orbit transfer, where the SWIFT-based spacecraft, which initially (at $t_0 = 0$) tracks a heliocentric circular orbit of radius $r_0 \triangleq r(t_0) = r_\oplus$, reaches a target circular orbit of given radius $r_f \triangleq r(t_f)$ at time t_f. It is assumed that at time t_0 the spacecraft leaves the Earth along a parabolic (escape) orbit. In addition, without loss of generality, the spacecraft's initial polar angle is set equal to zero, while the final value of

θ is left free, that is, it is an output of the optimization process. Accordingly, the initial and final constraints on the spacecraft state variables $\{r,\ \theta,\ v_r,\ v_\theta\}$ are

$$r(t_0) = r_\oplus \quad , \quad \theta(t_0) = 0 \quad , \quad v_r(t_0) = 0 \quad , \quad v_\theta(t_0) = \sqrt{\frac{\mu_\odot}{r_\oplus}} \tag{40}$$

$$r(t_f) = r_f \quad , \quad v_r(t_f) = 0 \quad , \quad v_\theta(t_f) = \sqrt{\frac{\mu_\odot}{r_f}}. \tag{41}$$

The orbit transfer is analyzed in an optimal framework [44–46], in which the trajectory is found by minimizing the flight time necessary for the spacecraft to reach the target orbit. This amounts to maximizing the performance index

$$J \triangleq -t_f, \tag{42}$$

where t_f coincides with the total flight time to be calculated. The optimal control problem is faced with an indirect approach [47,48], in which the Hamiltonian $\mathcal{H}$ is obtained from Equations (3), (4), (38) and (39) as

$$\mathcal{H} = \lambda_r\, v_r + \lambda_\theta\, v_\theta + \lambda_{v_r}\left[\frac{v_\theta^2}{r} - \frac{\mu_\odot}{r^2} + a_{D_\oplus}\left(\frac{r_\oplus}{r}\right)^2(1 + k\,\cos\alpha)\right] + \\ + \lambda_{v_\theta}\left[-\frac{v_r\, v_\theta}{r} + a_{D_\oplus}\left(\frac{r_\oplus}{r}\right)^2 k\,\sin\alpha\right], \tag{43}$$

where $\{\lambda_r,\ \lambda_\theta,\ \lambda_{v_r},\ \lambda_{v_\theta}\}$ are the variables adjoint to the spacecraft states. The time variation of the adjoint variables is described by the Euler–Lagrange equations [47,48],

$$\dot\lambda_r = -\frac{\partial\mathcal{H}}{\partial r}\ ,\ \dot\lambda_\theta = -\frac{\partial\mathcal{H}}{\partial\theta}\ ,\ \dot\lambda_{v_r} = -\frac{\partial\mathcal{H}}{\partial v_r}\ ,\ \dot\lambda_{v_\theta} = -\frac{\partial\mathcal{H}}{\partial v_\theta}, \tag{44}$$

whose explicit expressions are here omitted for the sake of brevity. It can be easily verified that $\dot\lambda_\theta = 0$ (in fact $\mathcal{H}$ does not explicitly depend on the polar angle), so that λ_θ is a constant of motion. Its value is found from the transversality condition that, in this case, reads

$$\lambda_\theta(t_f) = 0 \quad , \quad \mathcal{H}(t_f) = 1, \tag{45}$$

from which $\lambda_\theta = 0$ during the whole flight.

The optimal control law $\alpha = \alpha^\star(t)$, that is, the optimal time variation of the thrust angle, comes from the Pontryagin's maximum principle [48], according to which α must maximize the Hamiltonian at any time instant. Observing from Equation (43) that

$$\mathcal{H}' \triangleq a_{D_\oplus}\, k\left(\frac{r_\oplus}{r}\right)^2\left[\lambda_{v_r}\,\cos\alpha + \lambda_{v_\theta}\,\sin\alpha\right] \tag{46}$$

coincides with that part of $\mathcal{H}$ that explicitly depends on α, and recalling that the thrust angle modulus is upper constrained by $\alpha_{\max}$ of Equation (8), the optimal control law is found to be

$$\alpha^\star = \begin{cases} \alpha_{\max} & \text{if } \sigma > \alpha_{\max} \\ -\alpha_{\max} & \text{if } \sigma < -\alpha_{\max} \\ \sigma & \text{otherwise,} \end{cases} \tag{47}$$

where $\sigma \in (-\pi,\ \pi]$ rad is an auxiliary angle defined as

$$\sin\sigma \triangleq \frac{\lambda_{v_\theta}}{\sqrt{\lambda_{v_\theta}^2 + \lambda_{v_r}^2}} \quad , \quad \cos\sigma \triangleq \frac{\lambda_{v_r}}{\sqrt{\lambda_{v_\theta}^2 + \lambda_{v_r}^2}}. \tag{48}$$

The optimal control law for a SWIFT system is different from that of an ideal solar sail. This is clearly shown in Figure 8, which, with the aid of Sauer's results [37], compares the optimal thrust angle as a function of σ for an ideal solar sail and a SWIFT propulsion system with an aperture angle $\delta = 60$ deg and a contingency $\Delta\alpha = 0$.

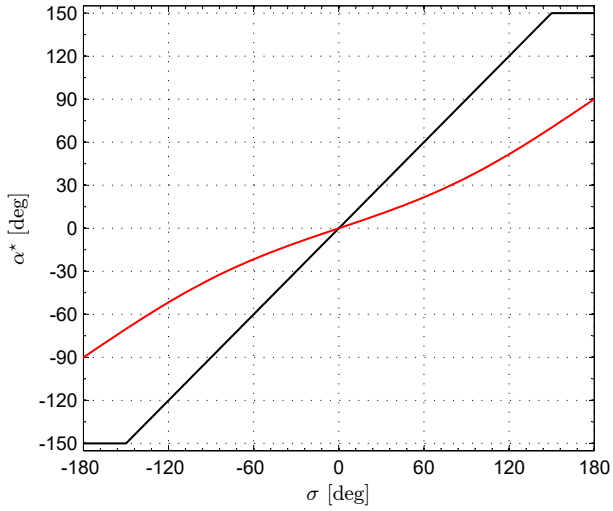

Figure 8. Comparison between the optimal control law SWIFT (black line) and an ideal flat solar sail (red line) when $\delta = 60$ deg and $\Delta\alpha = 0$, that is, $\alpha_{\max} = 150$ deg.

The associated two-point boundary value problem is described by the eight differential Equations (3), (4), (38), (39) and (44) with the eight boundary conditions given by Equations (40) and (41) and the first of Equation (45), while the last of Equation (45) allows the minimum flight time to be calculated. The two-point boundary value problem has been solved with a hybrid numerical technique that combines genetic algorithms with gradient-based methods [49]. The next section analyzes the results obtained by numerically solving the optimal control problem in a pair of typical mission scenarios.

4. Numerical Simulations and Mission Applications

The previous SWIFT thrust model is now used to evaluate the spacecraft propulsive performance for a given set of design parameters. To that end, we use the main assumptions made in the original work by Gemmer et al. [34], with a few changes. More precisely, the main differences between the data reported in Table 2 and those indicated in Ref. [34] are the values of $\{d,\ N_s\}$ that were originally chosen as $\{1\,\text{m},\ 1\}$. In addition, recall that in this work the thrust model accounts for the presence of a sort of "payload" mass term (which coincides with the term m_b in the current notation), a contingency angle $\Delta\alpha$, and a maximum thrust angle constraint, which are not considered in the simplified model discussed in Ref. [34].

The design parameters of the SWIFT-based spacecraft are summarized in Table 2, where the main spacecraft mass m_b is assumed to be 250 kg, while β is a trade-off value between flight-qualified solar panels (i.e., 10^{-3} kg/W) and cutting-edge photovoltaic (i.e., 5×10^{-2} kg/W) [34,50]. Using these design parameters, the spacecraft characteristics and its propulsive performance are those detailed in Table 3. In particular, according to Equation (8), the assumed values of δ and $\Delta\alpha$ provide $\alpha_{\max} = 90$ deg, so that the steerable propulsive force T has a non-negative radial component, as happens in a typical solar sail [16] or E-sail [22] mission scenario. This aspect is highlighted in Figure 9, which shows the SWIFT force bubble used in the numerical simulations at a distance $r = r_\oplus$ from the Sun. Note that, according to Equation (11), the value $k = 1$ gives a steerable thrust magnitude equal to D and an exhaust velocity of 400 km/s. The assumed value of v_{ex} is well above the current typical range, but it is consistent with the recent development in the area of electric

propulsion systems [51]. Figure 9 shows that in this case the maximum radial acceleration a_r is equal to twice the maximum transverse component a_θ.

Table 2. SWIFT propulsion system design parameters used in the thrust vector mathematical model.

Parameter	Value	Units
d	10	m
m_b	250	kg
N_e	100	–
N_s	4	–
R	3	km
r_w	2×10^{-5}	m
v_{ex}	400	km/s
β	2×10^{-3}	kg/W
δ	120	deg
$\Delta\alpha$	30	deg
ϕ_0	10	kV
ρ_{lb}	4×10^{-2}	kg/m

Table 3. Characteristics and propulsive performance of the SWIFT-based spacecraft used in the numerical simulations.

Parameter	Value	Units
$a_{D_\oplus}$	0.035	mm/s^2
$D_\oplus$	0.0552	N
m	1 582	kg
P	11.1	kW
k	1	–
$\alpha_{\max}$	90	deg

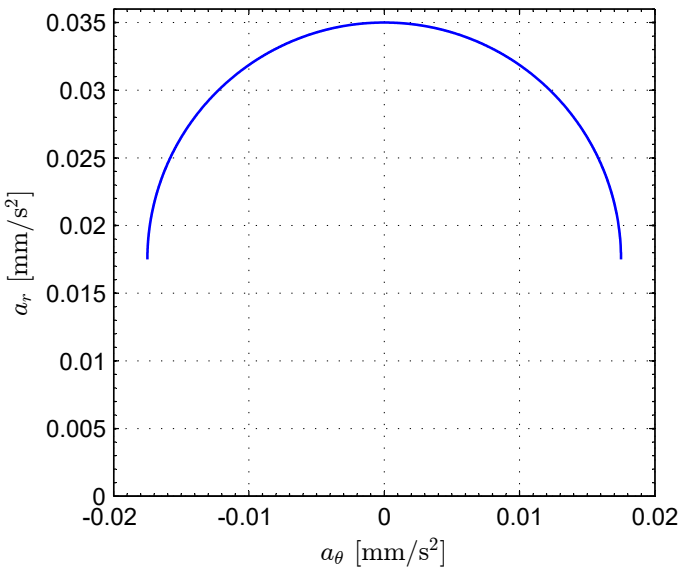

Figure 9. SWIFT force bubble when $r = r_\oplus$, $k = 1$, $\alpha_{\max} = 90$ deg and $a_{D_\oplus} = 0.035$ mm/s^2.

Case Study

Two specific mission applications are considered to estimate the optimal performance of a SWIFT-based spacecraft, the main characteristics of which are detailed in Table 3. In particular, an orbit raising with $r_f = r_{\male} \triangleq 1.524$ au, and an orbit lowering with $r_f = r_{\female} \triangleq 0.723$ au have been studied. Recalling that the radius of the initial circular orbit is $r_0 = r_{\oplus} = 1$ au, the case of $r_f = r_{\male}$ (or $r_f = r_{\female}$) is representative of a simplified, ephemeris-free, Earth–Mars (or Earth–Venus) interplanetary transfer in which the eccentricity and the inclination over the Ecliptic of both planetary orbits are neglected. The results of the numerical optimization for the Earth–Mars transfer give a minimum flight time that is slightly shorter than 8.1 years, with an optimal transfer trajectory that completes five revolutions around the Sun before reaching the target Mars orbit. This aspect is confirmed by Figure 10a, which shows the optimal transfer trajectory in a polar reference frame. According to Figure 10b, which shows the optimal time variation of the thrust angle, α reaches six times the maximum value $\alpha_{\max}$ with a mean value (over the entire transfer) of about 84 deg.

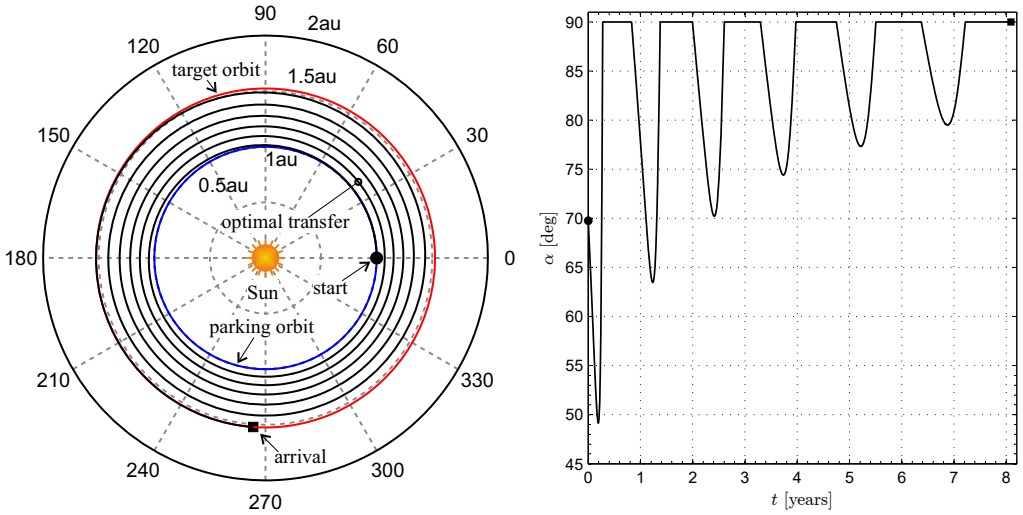

(**a**) Polar form of the transfer trajectory. (**b**) Optimal control law $\alpha = \alpha(t)$.

Figure 10. Optimal transfer trajectory and control angle history in an Earth–Mars transfer. Black circle (or square) refers to the start (or arrival) point.

The time variations of the spacecraft states $\{r, \theta, v_r, v_\theta\}$ are reassumed in Figure 11. Note that the radial spacecraft velocity v_r remains small during the whole transfer, so that the optimal transfer trajectory can be approximated with a sort of tight spiral connecting the initial and final (circular) orbits. This feature of the transfer trajectory is the result of a propulsive acceleration that is small, in comparison with the (local) Sun's gravitational acceleration. Figure 11 also shows that the time variation of the Sun–spacecraft distance r (or the transverse component of the inertial spacecraft velocity v_θ) may be thought of as a superposition of a secular increase (or decrease) and a short period of oscillation. As a result, the SWIFT system's performance is similar to that obtained using a solar sail [52–54], an E-sail [25], a Heliogyro [55], or a low-performance electric thruster [56,57] as a primary propulsion system.

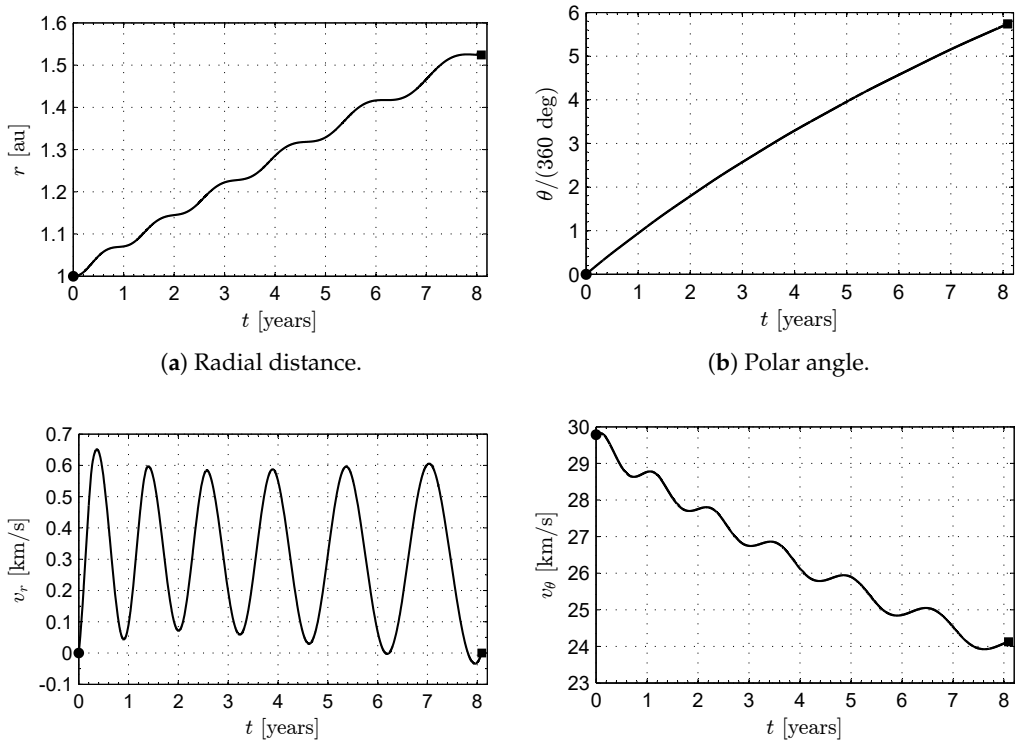

(**a**) Radial distance. (**b**) Polar angle.

(**c**) Radial component of velocity. (**d**) Transverse component of velocity.

Figure 11. Time variation of the spacecraft states in an Earth–Mars transfer. Black circle (or square) refers to the start (or arrival) point.

Similar considerations can be made for an Earth–Venus transfer (when $r_f = r_{\varphi}$), which is completed with a flight time of slightly above 3.6 years. In that case, the optimal transfer trajectory and the time variation of the thrust angle are shown in Figure 12, while the spacecraft states are reassumed in Figure 13. Note that $\alpha < 0$ during the entire transfer, that is, the steerable thrust T has a negative circumferential component. In that case, the value of $-\alpha_{\max}$ is reached five times, with a mean value of the thrust angle of about -80 deg.

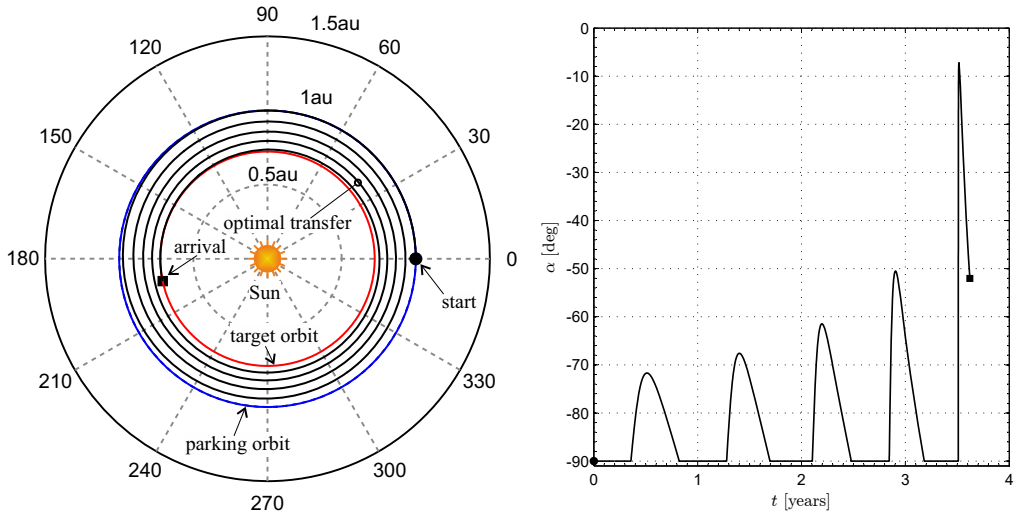

(**a**) Polar form of the transfer trajectory. (**b**) Optimal control law $\alpha = \alpha(t)$.

Figure 12. Optimal transfer trajectory and control angle history in an Earth–Venus transfer. Black circle (or square) refers to the start (or arrival) point.

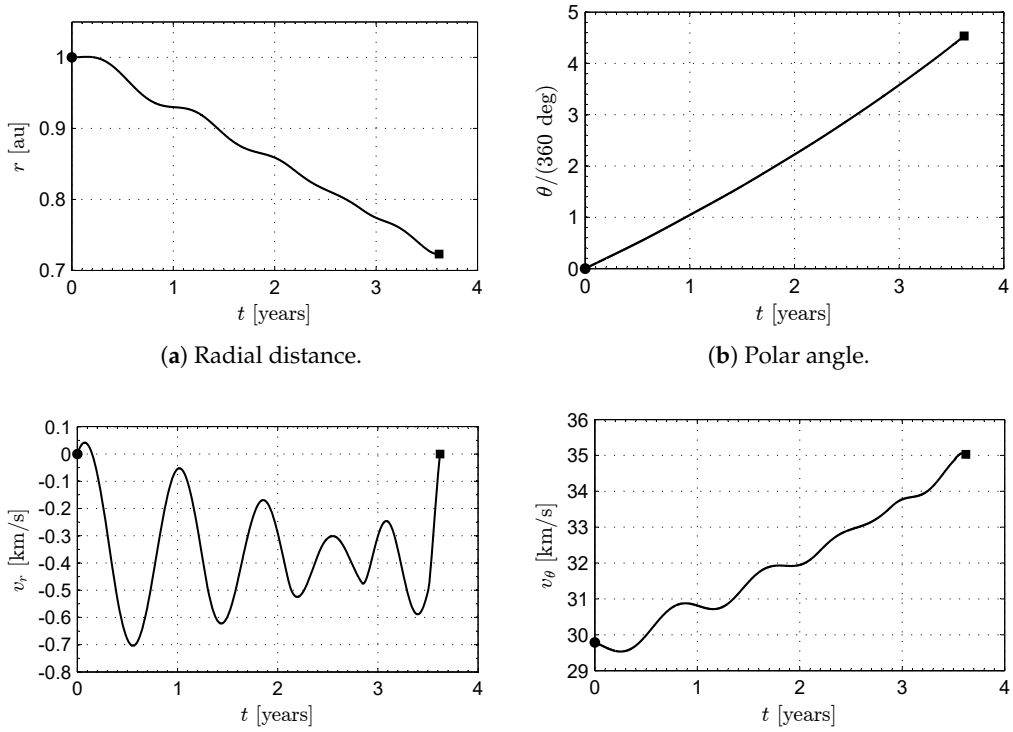

(**a**) Radial distance. (**b**) Polar angle.

(**c**) Radial component of velocity. (**d**) Transverse component of velocity.

Figure 13. Time variation of the spacecraft states in an Earth–Venus transfer. Black circle (or square) refers to the start (or arrival) point.

5. Conclusions

This paper has analyzed the performance of a SWIFT-based spacecraft in a heliocentric and two-dimensional mission scenario. In particular, an improved version of the thrust vector mathematical model has been discussed with the aim of obtaining a set of analytical equations useful for a preliminary trajectory analysis. The optimal control law has been obtained with an indirect approach, and the corresponding two-point boundary value problem has been solved using a hybrid numerical technique. The numerical results show that the typical propulsive performance of a SWIFT-based spacecraft, in a simplified interplanetary trajectory, provides a minimum flight time of some years for a mission towards Mars (or Venus) without ephemeris constraints. These numbers, which are comparable to more conventional propellantless systems such as solar sails or E-sails, prevents the use of this propulsion concept from a manned interplanetary mission, as expected. However, the intrinsic characteristic of a SWIFT propeller of providing a continuous thrust for a long period of time allows this propulsion system to be an interesting option in advanced high-energy missions such as the generation of artificial equilibrium points or displaced non-Keplerian orbits. These two latter applications are the focus of our current research and represent the natural extension of this work.

Author Contributions: Conceptualization, A.A.Q.; methodology, A.A.Q.; software, A.A.Q. and L.N.; writing—original draft preparation, A.A.Q. and L.N.; writing—review and editing, G.M. and M.B. All authors have read and agreed to the published version of the manuscript.

Funding: This work is partly supported by the University of Pisa, Progetti di Ricerca di Ateneo (Grant no. PRA_2022_1).

Institutional Review Board Statement: Not applicable.

Informed Consent Statement: Not applicable.

Data Availability Statement: Not applicable.

Conflicts of Interest: The authors declare no conflict of interest.

Abbreviations

Notation	
A	SWIFT cone base area [m^2]
$a_{D_\oplus}$	design parameter; see Equation (16) [mm/s^2]
$\boldsymbol{a}$	propulsive acceleration vector [mm/s^2]
$a_{\max}$	maximum propulsive acceleration magnitude [mm/s^2]
a_r	radial component of $\boldsymbol{a}$ [mm/s^2]
a_θ	transverse component of $\boldsymbol{a}$ [mm/s^2]
D	radial thrust ("drag") [N]
d	spacing between circular conducting wires [m]
e	elementary charge [C]
H	SWIFT cone height [m]
$\mathcal{H}$	Hamiltonian
k	dimensionless design parameter; see Equation (11)
$k^\star$	critical value of k; see Equation (37)
$\hat{\boldsymbol{i}}_r$	radial unit vector
$\hat{\boldsymbol{i}}_\theta$	circumferential unit vector
J	performance index
L_s	total length of structural elements [m]
L_w	total length of conducting wires [m]
m	total spacecraft mass [kg]
m_b	spacecraft main body mass [kg]
m_e	electron mass [kg]
m_p	proton mass [kg]
m_{ps}	SWIFT power generation system mass [kg]
m_s	SWIFT structure mass [kg]
m_w	SWIFT wires total mass [kg]
N_c	number of circular conducting wires
N_e	number of straight conducting wires
N_s	number of radial support booms
n_{sw}	solar wind density [particles/m^3]
$n_\oplus$	value of n_{sw} at 1 au from the Sun
O	Sun's center of mass
P	total power required by the SWIFT [W]
P_{ex}	power required by ion acceleration [W]
P_w	power required by wire grid [W]
R	SWIFT cone base radius [m]
r	Sun-spacecraft radial distance [au]
$\boldsymbol{r}$	spacecraft position vector [au]
r_w	conducting wire radius [m]
$r_\oplus$	reference distance [1 au]
T	steerable thrust [N]
t	time [days]
$\mathcal{T}$	polar reference frame
$\boldsymbol{v}$	spacecraft velocity vector [km/s]
v_r	radial component of the spacecraft velocity [km/s]
v_{sw}	solar wind velocity [km/s]
v_{ex}	exhaust velocity [km/s]
v_θ	transverse component of the spacecraft velocity [km/s]
α	thrust angle [deg]
$\alpha^\star$	optimal thrust angle [deg]
$\Delta\alpha$	contingency value [deg]

β	power system specific mass [kg/W]
δ	SWIFT cone aperture [deg]
ϕ_0	conducting wire electric potential [V]
λ_r	variable adjoint to r
λ_{v_r}	variable adjoint to v_r
λ_{v_θ}	variable adjoint to v_θ
λ_θ	variable adjoint to θ
$\mu_\odot$	Sun's gravitational parameter [km^3/s^2]
ρ_{lb}	support boom linear density [kg/m]
ρ_w	conducting wire density [kg/m^3]
θ	spacecraft polar angle [deg]
Subscripts	
0	initial, parking orbit
f	final, target orbit
♂	Mars
♀	Venus
ss	ideal flat solar sail

References

1. Jacobson, R.A.; Thornton, C.L. Elements of solar sail navigation with application to a Halley's comet rendezvous. *J. Guid. Control Dyn.* **1978**, *1*, 365–371. [CrossRef]
2. Quarta, A.A.; Mengali, G.; Janhunen, P. Electric sail option for cometary rendezvous. *Acta Astronaut.* **2016**, *127*, 684–692. [CrossRef]
3. Hughes, G.W.; McInnes, C.R. Small-body encounters using solar sail propulsion. *J. Spacecr. Rocket.* **2004**, *41*, 140–150. [CrossRef]
4. Quarta, A.A.; Mengali, G.; Janhunen, P. Electric sail for a near-Earth asteroid sample return mission: Case 1998 KY26. *J. Aerosp. Eng.* **2014**, *27*, 4014031. [CrossRef]
5. Slavinskis, A.; Janhunen, P.; Toivanen, P.; Muinonen, K.; Penttilä, A.; Granvik, M.; Kohout, T.; Gritsevich, M.; Pajusalu, M.; Sunter, I.; et al. Nanospacecraft fleet for multi-asteroid touring with electric solar wind sails. In Proceedings of the IEEE Aerospace Conference, Big Sky, MT, USA, 3–10 March 2018; pp. 1–20. [CrossRef]
6. Dandouras, I.; Pirard, B.; Prado, J.Y. High performance solar sails for linear trajectories and heliostationary missions. *Adv. Space Res.* **2004**, *34*, 198–203. [CrossRef]
7. Quarta, A.A.; Mengali, G. Optimal solar sail transfer to linear trajectories. *Acta Astronaut.* **2013**, *82*, 189–196. . 1016/j.actaastro.2012.03.005. [CrossRef]
8. Gong, S.; Li, J. Solar sail heliocentric elliptic displaced orbits. *J. Guid. Control Dyn.* **2014**, *37*, 2021–2025. . 1.G000660. [CrossRef]
9. Niccolai, L.; Quarta, A.A.; Mengali, G. Electric sail elliptic displaced orbits with advanced thrust model. *Acta Astronaut.* **2017**, *138*, 503–511. [CrossRef]
10. Niccolai, L.; Anderlini, A.; Mengali, G.; Quarta, A.A. Electric sail displaced orbit control with solar wind uncertainties. *Acta Astronaut.* **2019**, *162*, 563–573. [CrossRef]
11. Bassetto, M.; Quarta, A.A.; Mengali, G. Magnetic sail-based displaced non-Keplerian orbits. *Aerosp. Sci. Technol.* **2019**, *92*, 363–372. [CrossRef]
12. Aliasi, G.; Mengali, G.; Quarta, A.A. Artificial equilibrium points for a generalized sail in the circular restricted three-body problem. *Celest. Mech. Dyn. Astron.* **2011**, *110*, 343–368. [CrossRef]
13. Niccolai, L.; Caruso, A.; Quarta, A.A.; Mengali, G. Artificial collinear Lagrangian point maintenance with electric solar wind sail. *IEEE Trans. Aerosp. Electron. Syst.* **2020**, *56*, 4467–4477. [CrossRef]
14. Bianchi, C.; Niccolai, L.; Mengali, G.; Quarta, A.A. Collinear artificial equilibrium point maintenance with a wrinkled solar sail. *Aerosp. Sci. Technol.* **2021**, *119*, 1–14. [CrossRef]
15. Zeng, X.; Gong, S.; Li, J.; Alfriend, K.T. Solar sail body-fixed hovering over elongated asteroids. *J. Guid. Control Dyn.* **2016**, *39*, 1223–1231. [CrossRef]
16. McInnes, C.R. *Solar Sailing: Technology, Dynamics and Mission Applications*; Springer: Berlin, Germany, 1999; pp. 171–196. [CrossRef]
17. Fu, B.; Sperber, E.; Eke, F. Solar sail technology—A state of the art review. *Prog. Aerosp. Sci.* **2016**, *86*, 1–19. [CrossRef]
18. Bovesecchi, G.; Corasaniti, S.; Costanza, G.; Tata, M.E. A novel self-deployable solar sail system activated by shape memory alloys. *Aerospace* **2019**, *6*, 78. [CrossRef]
19. Zhang, F.; Gong, S.; Baoyin, H. Three-axes attitude control of solar sail based on shape variation of booms. *Aerospace* **2021**, *8*, 198. [CrossRef]
20. Zou, J.; Li, D.; Wang, J.; Yu, Y. Experimental study of measuring the wrinkle of solar sails. *Aerospace* **2022**, *9*, 289. [CrossRef]
21. Janhunen, P. Electric sail for spacecraft propulsion. *J. Propuls. Power* **2004**, *20*, 763–764. [CrossRef]
22. Bassetto, M.; Niccolai, L.; Quarta, A.A.; Mengali, G. A comprehensive review of Electric Solar Wind Sail concept and its applications. *Prog. Aerosp. Sci.* **2022**, *128*, 100768. [CrossRef]

23. Huo, M.Y.; Mengali, G.; Quarta, A.A. Electric sail thrust model from a geometrical perspective. *J. Guid. Control Dyn.* **2018**, *41*, 735–741. [CrossRef]
24. Bassetto, M.; Quarta, A.A.; Mengali, G.; Cipolla, V. Spiral trajectories induced by radial thrust with applications to generalized sails. *Astrodynamics* **2020**, *5*, 121–137. [CrossRef]
25. Quarta, A.A.; Mengali, G.; Bassetto, M.; Niccolai, L. Optimal circle-to-ellipse orbit transfer for Sun-facing E-sail. *Aerospace* **2022**, *9*, 671. [CrossRef]
26. Forward, R.L. Solar Photon Thrustor. *J. Spacecr. Rocket.* **1990**, *27*, 411–416. [CrossRef]
27. Mengali, G.; Quarta, A.A. Earth escape by ideal sail and solar-photon thrustor spacecraft. *J. Guid. Control Dyn.* **2004**, *27*, 1105–1108. [CrossRef]
28. Mengali, G.; Quarta, A.A. Time-optimal three-dimensional trajectories for solar photon thruster spacecraft. *J. Spacecr. Rocket.* **2005**, *42*, 379–381. [CrossRef]
29. Mengali, G.; Quarta, A.A. Compound solar sail with optical properties: Models and performance. *J. Spacecr. Rocket.* **2006**, *43*, 239–245. [CrossRef]
30. Fieseler, P.; Anderson, K.R.; Cable, V. Critical look at the solar photon thruster concept. *J. Spacecr. Rocket.* **2015**, *52*, 1152–1162. [CrossRef]
31. Gemmer, T.R.; Mazzoleni, A.P. Introduction and Performance Analysis of the Solar Wind Ion Focusing Thruster (SWIFT). In Proceedings of the 65th International Astronautical Congress, Toronto, ON, Canada, 29 September–3 October 2014; Paper IAC-14,C4,8,1,x24646.
32. Gemmer, T.R.; Mazzoleni, A.P. Solar wind ion focusing thruster (SWIFT) Orbital Performance Analysis. In Proceedings of the 66th International Astronautical Congress, Jerusalem, Israel, 12–16 October 2015.
33. Gemmer, T.R.; Mazzoleni, A.P. Comparative orbital performance study of a solar wind ion focusing thruster (SWIFT). In Proceedings of the 67th International Astronautical Congress, Guadalajara, Mexico, 26–30 September 2016; Paper IAC-16,C4,8,8,x33664.
34. Gemmer, T.R.; Yoder, C.D.; Mazzoleni, A.P. Performance Analysis and Parametric Studies of the Solar Wind Ion Focusing Thruster (SWIFT) for Interplanetary Travel. *J. Br. Interplanet. Soc.* **2021**, *74*, 30–40.
35. Ross, I.M. *A Primer on Pontryagin's Principle in Optimal Control*; Collegiate Publishers : San Francisco, CA, USA, 2015; Chapter 2, pp. 127–129. ISBN 9780984357116.
36. Lawden, D.F. *Optimal Trajectories for Space Navigation*; Butterworths & Co.: London, UK, 1963; pp. 54–60.
37. Sauer, C.G., Jr. Optimum Solar-Sail Interplanetary Trajectories. In Proceedings of the AIAA/AAS Astrodynamics Conference , San Francisco, CA, USA, 18–20 August 1976. [CrossRef]
38. Gallana, L.; Fraternale, F.; Fosson, S.M.; Magli, E.; Opher, M.; Richardson, J.D.; Tordella, D. Voyager 2 solar plasma and magnetic field spectral analysis for intermediate data sparsity. *J. Geophys. Res. A Space Phys.* **2016**, *121*, 3905–3919. [CrossRef]
39. Phillips, J.L.; Bame, S.J.; Barnes, A.; Barraclough, B.M.; Feldman, W.C.; Goldstein, B.E. Ulysses solar wind plasma observations from pole to pole. *Geophys. Res. Lett.* **1995**, *22*, 3301–3304. [CrossRef]
40. Stone, E.C.; Frandsen, A.M.; Mewaldt, R.A.; Christian, E.R.; Margolies, D.; Ormes, J.F. The Advanced Composition Explorer. *Space Sci. Rev.* **1998**, *86*, 1–22. ._1. [CrossRef]
41. Mengali, G.; Quarta, A.A.; Circi, C.; Dachwald, B. Refined solar sail force model with mission application. *J. Guid. Control Dyn.* **2007**, *30*, 512–520. [CrossRef]
42. Wright, J.L. *Space Sailing*; Gordon and Breach Science Publishers : Amsterdam, The Netherlands, 1992.
43. Bassetto, M.; Quarta, A.A.; Mengali, G.; Cipolla, V. Trajectory analysis of a Sun-facing solar sail with optical degradation. *J. Guid. Control Dyn.* **2020**, *43*, 1727–1732. [CrossRef]
44. Antonakis, A.; Nikolaidis, T.; Pilidis, P. Multi-objective climb path optimization for aircraft/engine integration using particle swarm optimization. *Appl. Sci.* **2017**, *7*, 469. [CrossRef]
45. Morante, D.; Sanjurjo Rivo, M.; Soler, M. A Survey on Low-Thrust Trajectory Optimization Approaches. *Aerospace* **2021**, *8*, 88. [CrossRef]
46. Jia, F.; Peng, Q.; Zhou, W.; Li, X. Integrated design of Moon-to-Earth transfer trajectory considering re-entry constraints. *Appl. Sci.* **2022**, *12*, 8716. [CrossRef]
47. Bryson, A.E.; Ho, Y.C. *Applied Optimal Control*; Hemisphere Publishing Corporation: New York, NY, USA, 1975; Chapter 2, pp. 71–89. ISBN 0-891-16228-3.
48. Stengel, R.F. *Optimal Control and Estimation*; Dover Publications, Inc. : New York, NY, USA, 1994; pp. 222–254.
49. Mengali, G.; Quarta, A.A. Optimal three-dimensional interplanetary rendezvous using nonideal solar sail. *J. Guid. Control Dyn.* **2005**, *28*, 173–177. [CrossRef]
50. Shiu, K.T.; Zimmerman, J.; Wang, H.; Forrest, S.R. Ultrathin film, high specific power InP solar cells on flexible plastic substrates. *Appl. Phys. Lett.* **2009**, *95*, 223503. [CrossRef]
51. Brophy, J.R.; Polk, J.E.; Goebel, D.M. Development of a 50,000-s, Lithium-fueled, Gridded Ion Thruster. In Proceedings of the 35th International Electric Propulsion Conference, Atlanta, GA, USA, 8–15 October 2017; Paper IEPC-2017-042.
52. Caruso, A.; Quarta, A.A.; Mengali, G. Comparison Between Direct and Indirect Approach to Solar Sail Circle-to-circle Orbit Raising Optimization. *Astrodynamics* **2019**, *3*, 273–284. [CrossRef]
53. Quarta, A.A.; Mengali, G. Approximate Solutions to Circle-to-Circle Solar Sail Orbit Transfer. *J. Guid. Control Dyn.* **2013**, *36*, 1866–1890. [CrossRef]

54. Quarta, A.A.; Mengali, G. Semi-Analytical Method for the Analysis of Solar Sail Heliocentric Orbit Raising. *J. Guid. Control Dyn.* **2012**, *35*, 330–335. [CrossRef]
55. Bassetto, M.; Quarta, A.A.; Caruso, A.; Mengali, G. Optimal heliocentric transfers of a Sun-facing heliogyro. *Aerosp. Sci. Technol.* **2021**, *119*, 107094. [CrossRef]
56. Mengali, G.; Quarta, A.A. Trajectory design with hybrid low-thrust propulsion system. *J. Guid. Control Dyn.* **2007**, *30*, 419–426. [CrossRef]
57. Mengali, G.; Quarta, A.A. Optimal trade studies of interplanetary electric propulsion missions. *Acta Astronaut.* **2008**, *62*, 657–667. [CrossRef]